Inorg. Chem. **2006**, *45*, 3499–3509

Molecular and Electronic Structures of Oxo-bis(benzene-1,2-dithiolato)chromate(V) Monoanions. A Combined Experimental and Density Functional Study

Ruta Kapre,[†] Kallol Ray,[†] Isabelle Sylvestre,[†] Thomas Weyhermüller,[†] Serena DeBeer George,[‡] Frank Neese,*[,†] and Karl Wieghardt*[,†]

Max-Planck Institut für Bioanorganische Chemie, Stiftstrasse 34-36, D-45470 Mülheim an der Ruhr, Germany, and Stanford Synchrotron Radiation Laboratory, SLAC, Stanford University, Stanford, California 94309

Received October 25, 2005

Two oxo-bis(benzene-1,2-dithiolato)chromate(V) complexes, namely, $[CrO(L^{Bu})_2]^{1-}$ and $[CrO(L^{Me})_2]^{1-}$, have been synthesized and studied by UV–vis, EPR, magnetic circular dichroism (MCD), and X-ray absorption spectroscopy and by X-ray crystallography; their electro- and magnetochemistries are reported. H_2L^{Bu} represents the pro-ligand 3,5-di-*tert*-butylbenzene-1,2-dithiol, and H_2L^{Me} is the corresponding 4-methyl-benzene-1,2-dithiol. A structural feature of interest for both the complexes is the folding of the dithiolate ligands about the S–S vector providing C_s symmetry to the complexes. Geometry optimizations using all-electron density functional theory with scalar relativistic corrections at the second-order Douglas–Kroll–Hess (DKH2) and zeroth-order regular approximation (ZORA) levels result in excellent agreement with the experimentally determined structures and electronic and S K-edge X-ray absorption spectra. From DFT calculations, the C_s instead of C_{2v} symmetry for the complexes is attributed to the strong S(3p) → Cr($3d_{x^2-y^2}$) π-donation in C_s geometry providing additional stability to the complexes.

Introduction

Stable oxochromium(V) complexes are attractive synthetic targets for inorganic chemists because of their applications in the fields of chemistry,[1] chemical biology,[2] and nuclear physics.[3] Perhaps the most prominent reactivity of such complexes is their ability to catalyze the epoxidation of alkenes by a formal oxygen atom transfer reaction (Scheme 1), which indicates that the oxo ligand may acquire considerable electrophilic character. Experimental support for the crucial role played by reactive oxochromium(V) intermediates during the epoxidation of olefins was provided initially by Groves et al.[4] Kochi et al later reported the first structure determination of a catalytically active oxochromium(V) complex.[5] A number of similar complexes showing interesting catalytic[6] and biochemical properties[7] have subsequently been reported in the literature.

Scheme 1

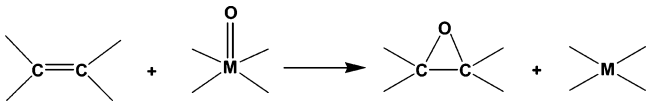

An understanding of the electronic structures of well-characterized oxochromium(V) complexes is essential to

* To whom correspondence should be addressed. E-mail: wieghardt@mpi-muelheim.mpg.de (K.W.); neese@mpi-muelheim.mpg.de (F.N.).
[†] Max-Planck Institut für Bioanorganische Chemie.
[‡] Stanford Synchrotron Radiation Laboratory.

(1) (a) Rocek, J.; Radkowski, A. E. *J. Am. Chem. Soc.* **1968**, *90*, 2986. (b) Rahman, M.; Rocek, J. *J. Am. Chem. Soc.* **1971**, *93*, 5455. (c) Rocek, J.; Radkowski, A. E. *J. Am. Chem. Soc.* **1973**, *95*, 7123. (d) Hasan, F.; Rocek, J. *Terahedron* **1974**, *30*, 21. (e) Rocek, J.; Ng, C.-S. *J. Am. Chem. Soc.* **1974**, *96*, 1522. (f) Rocek, J.; Ng, C.-S. *J. Am. Chem. Soc.* **1974**, *96*, 2840. (g) Hasan, F.; Rocek, J. *J. Am. Chem. Soc.* **1976**, *98*, 6574.
(2) (a) Connett, P.; Wetterhahn, K. E. *Struct. Bonding (Berlin)* **1983**, *54*, 93. (b) Levina, A.; Barr-David, G.; Codd, R.; Lay, P. A.; Dixon, N. E.; Hammershoi, A.; Hendry, P. *Chem. Res. Toxicol.* **1999**, *12*, 371 and references therein.
(3) (a) Glättli, H.; Odehnal, M.; Ezratty, J.; Malinovsky, A.; Abragam, A. *Phys. Lett. A* **1969**, *29*, 250. (b)Masaike, A.; Glättli, H.; Ezratty, J.; Malinovsky, A. *Phys. Lett. A* **1969**, *30*, 63. (c)Borghini, M.; Chamberlain, O.; Fuzesy, R. Z.; Gorn, W.; Morehouse, C. C.; Powell, T.; Robrish, P.; Rock, S.; Shannon, S.; Shapiro, G.; Weisberg, H. *Nucl. Instrum. Methods* **1970**, *84*, 168.
(4) Groves, J. T.; Kruper, W. J., Jr. *J. Am. Chem. Soc.* **1979**, *101*, 7613.
(5) Siddall, T. L.; Miyaura, N.; Huffman, J. C.; Kochi, J. K. *J. Chem. Soc., Chem. Commun.* **1983**, 1185.
(6) (a) Samsel, E. G.; Srinivisan, K.; Kochi, J. K. *J. Am. Chem. Soc.* **1985**, *107*, 7606. (b) Srinivasan, K.; Kochi, J. K. *Inorg. Chem.* **1985**, *24*, 4671.

10.1021/ic051844s CCC: $33.50
Published on Web 02/17/2006

interpreting their spectroscopic and catalytic properties. However, in contrast to the more intensely studied oxomolybdenum(V) analogues,[10] little is known about their electronic structure, except for EPR[8] and Cr K-edge X-ray absorption studies.[8b,9] In this paper, we consider in detail the physical properties of $[(n\text{-Bu})_4\text{N}][\text{CrO}(\text{L}^{\text{Bu}})_2]$(**1**), $[(\text{Ph})_4\text{As}][\text{CrO}(\text{L}^{\text{Bu}})_2]$(**1a**), and $[(n\text{-Bu})_4\text{N}][\text{CrO}(\text{L}^{\text{Me}})_2]$ (**2**) complexes; L^{Bu} represents the 3,5-di-*tert*-butyl-1,2-benzene-dithiolato dianion, and L^{Me} represents the 4-methyl-1,2-benzenedithiolato dianion. Complex **2** was initially synthesized by Gray et al.[11] in 1966, and its EPR spectrum was also reported. This represents the only example of a Cr(V) ion in a bis(dithiolene) environment. However, the chemistry of this species has remained unexplored. Here we report the crystal structure of **1a**·$2\text{CH}_3\text{CN}$ and **2** at 100 K. The complexes have been studied spectroscopically (electronic absorption, EPR, magnetic circular dichroism (MCD), and X-ray absorption spectroscopy (XAS)) and by cyclic voltammetry (CV) and density functional theoretical (DFT) calculations. The question of the innocent versus noninnocent nature of the benzene-1,2-dithiolato ligands in **1** and **2** has also been addressed on the basis of the crystallographic and spectroscopic markers[12] established for the detection of the dithiobenzosemiquinonato(1−) radical ions in coordination complexes.

Experimental Section

Synthesis of Complexes. 3,5-Di-*tert*-butyl-1,2-benzenedithiol, $\text{H}_2[\text{L}^{\text{Bu}}]$, was synthesized as described in the literature.[13] 4-Methyl-1,2-benzenedithiol, $\text{H}_2[\text{L}^{\text{Me}}]$, is commercially available (Aldrich). K_2CrO_4 and *trans*-$[\text{Cr}(\text{H}_2\text{O})_4\text{Cl}_2]\text{Cl}$ (for the Cr K-edge XAS measurements) were purchased from Strem and were used without further purification. $\text{CrCl}_3(\text{THF})_3$ and CrCl_2 were obtained from Aldrich. All solvents were dried and distilled before use.

$[\text{N}(n\text{-Bu})_4][\text{CrO}(\text{L}^{\text{Bu}})_2]$ (1). $\text{CrCl}_3(\text{THF})_3$ (0.093 g, 0.250 mmol) was added to a solution of 3,5-di-*tert*-butyl-1,2-benzenedithiol (0.126 g, 0.500 mmol) in 25 mL of MeCN, followed by the addition of Et_3N (0.300 mL, 3.000 mmol) under argon. The green solution was stirred in air for 60 min. The color changed from green to red-brown. $[\text{N}(n\text{-Bu})_4]\text{Br}$ (0.082 g, 0.250 mmol) was then added, and the reaction mixture was stirred for another 60 min. Keeping the resultant solution under a continuous flow of argon overnight resulted in the separation of shiny deep brown crystals, which were isolated by filtration. Yield: 0.122 g (60%). Anal. Calcd for $\text{C}_{44}\text{H}_{76}\text{S}_4\text{OCrN}$: C, 64.8; H, 9.4; N, 1.7. Found: C, 64.6; H, 9.3; N, 1.7. Electrospray mass spectrum (CH_2Cl_2 solution) positive and negative ion mode: *m*/*z* 572.3 $\{\text{CrO}(\text{L}^{\text{Bu}})_2\}^-$; 242.3 $\{\text{N}(n\text{-Bu})_4\}^+$. IR (KBr): $\bar{\nu}$ 967 (Cr═O).

Single crystals of $[\text{As}(\text{Ph})_4][\text{CrO}(\text{L}^{\text{Bu}})_2]\cdot 2\text{CH}_3\text{CN}$ (**1a**·$2\text{CH}_3\text{CN}$) suitable for X-ray crystallography were obtained using $[\text{As}(\text{Ph})_4]$Br in the above reaction instead of $[\text{N}(n\text{-Bu})_4]$Br.

$[\text{N}(n\text{-Bu})_4][\text{CrO}(\text{L}^{\text{Me}})_2]$ (2). A solution of $\text{H}_2[\text{L}^{\text{Me}}]$ (0.628 mg, 3.142 mmol) and NaOMe (1.450 g, 12.000 mmol) in 50 mL of MeOH was added dropwise to a light blue solution of CrCl_2 (0.190 mg, 1.550 mmol) in 50 mL of MeOH under an argon atmosphere at ambient temperature. The solution was stirred in air for 2 min, and the resultant blue-violet solution was treated with a solution of $[(n\text{-Bu})_4\text{N}]\text{Br}$ (1.011 g, 3.140 mmol) in 20 mL of MeOH. A violet-brown powder precipitated from the solution over the course of 2 days. It was redissolved in 15 mL of THF. After filtration, the filtrate was kept at −20 °C. Single crystals suitable for X-ray crystallography were obtained within 20 days. Yield: 0.412 g (43%). Electrospray mass spectrum (CH_2Cl_2 solution) positive and negative ion mode: *m*/*z* 376 $\{\text{CrO}(\text{L}^{\text{Me}})_2\}^-$; 242.3 $\{\text{N}(n\text{-Bu})_4\}^+$. IR (KBr): $\bar{\nu}$ 964 (Cr═O). Anal. Calcd for $\text{C}_{30}\text{H}_{48}\text{CrNOS}_4$: C, 58.2; H, 7.8; N, 2.3. Found: C, 58.0; H, 7.6; N, 2.2.

X-ray Crystallographic Data Collection and Refinement of the Structures. Brown single crystals of **1a**·$2\text{CH}_3\text{CN}$ and **2** were coated with perfluoropolyether, picked up with a glass fiber and immediately mounted in the nitrogen cold stream of the diffractometer to prevent loss of solvent. A Nonius Kappa-CCD diffractometer equipped with a Mo-target rotating-anode X-ray source and a graphite monochromator (Mo Kα, λ = 0.71073 Å) was used. Final cell constants were obtained from least-squares fits of all measured reflections. The crystal faces of **1a** were indexed, and the Gaussian-type correction routine embedded in XPREP[14] was used to correct for absorption. The data for **2** were left uncorrected. The structures were readily solved by direct and Patterson methods and subsequent difference Fourier techniques. The Siemens SHELXTL[14] software package was used for solution and artwork of the structure,and SHELXL97[15] was used for the refinement. All non-hydrogen atoms were refined anisotropically. Hydrogen atoms were placed at calculated positions and refined as riding atoms with isotropic displacement parameters. Crystallographic data of the compounds are listed in Table 1. Disorder was found in both structures, and split atom models were refined (see Figure S1). Residual electron density in the core of **1a** showed that the complex contains a minor second component with an occupation factor of about 0.17. The structure of this component can be deduced from the major part by inversion of the CrS_4O pyramidal unit. Identical thermal displacement parameters for both components were used, and Cr−S distances were restrained to be equal within the errors for the split atoms Cr(1), O(1), S(1), and S(2). The methyl group

(7) (a) Sugden, K. D.; Wetterhahn, K. E. *J. Am. Chem. Soc*. **1996**, *118*, 10811. (b) Farrell, R. P.; Lay, P. A.; Levina, A.; Maxwell, I. A.; Bramley, R.; Brumby, S.; Ji, J.-Y. *Inorg. Chem.* **1998**, *37*, 3159. (c) Codd, R.; Dillon, C. T.; Lay, P. A. *Coord. Chem. Rev.* **2001**, *216*−*217*, 533. (d) Levina, A.; Codd, R.; Dillon, C. T.; Lay, P. A. *Prog. Inorg. Chem*. **2003**, *51*, 145.

(8) (a) Pattison, D. I.; Lay, P. A.; Davies, M. J. *Inorg. Chem.* **2000**, *39*, 2729. (b) Levina, A.; Zhang, L.; Lay, P. A. *Inorg. Chem.* **2003**, *42*, 767.

(9) (a) Codd, R.; Levina, A.; Zhang, L.; Hambley, T. W.; Lay, P. A. *Inorg. Chem.* **2000**, *39*, 990. (b) Levina, A.; Codd, R.; Foran, G. J.; Hambley, T. W.; Maschmeyer, T.; Masters, A. F.; Lay, P. A. *Inorg. Chem.* **2004**, *43*, 1046.

(10) (a) Boyde, S.; Ellis, S. R.; Garner, C. D.; Clegg, W. *J. Chem. Soc., Chem. Commun.* **1986**, 1541. (b) McMaster, J.; Carducci, M. D.; Yang, Y.-S.; Solomon, E. I.; Enemark, J. H. *Inorg. Chem.* **2001**, *40*, 687. (c) Carducci, M. D.; Brown, C.; Solomon, E. I.; Enemark, J. H. *J. Am. Chem. Soc.* **1994**, *116*, 11856. (d) Musgrave, K. B.; Donahue, J. P.; Lorber, C.; Holm, R. H.; Hedman, B.; Hodgson, K. O. *J. Am. Chem. Soc.* **1999**, *121*, 10297. (e) Astashkin, A. V.; Neese, F.; Raitsimring, A. M.; Cooney, J. J. A.; Bultman, E.; Enemark, J. H. *J. Am. Chem. Soc.* **2005**, *44*, 1290.

(11) Steifel, E. I.; Eisenberg, R.; Rosenberg, R. C.; Gray, H. B. *J. Am. Chem. Soc.* **1966**, *88*, 2956.

(12) (a) Ray, K.; Weyhermüller, T.; Goossens, A.; Crajé, M. W. J.; Wieghardt, K. *Inorg. Chem.* **2003**, *42*, 4082. (b) Ray, K.; Bill, E.; Weyhermüller, T.; Wieghardt, K. *J. Am. Chem. Soc.* **2005**, *127*, 5641. (c) Ray, K.; Begum, A.; Weyhermüller, T.; Piligkos, S.; Slageren, J. V.; Neese, F.; Wieghardt, K. *J. Am. Chem. Soc.* **2005**, *127*, 4403. (d) Ray, K.; Weyhermüller, T.; Neese, F.; Wieghardt, K. *Inorg. Chem.* **2005**, *44*, 5345.

(13) (a) Sellmann, D.; Freyberger, G.; Eberlein, R.; Böhlen, E.; Huttner, G.; Zsolnai, L. *J. Organomet. Chem.* **1987**, *323*, 21. (b) Sellmann, D.; Käppler, O. *Z. Naturforsch.* **1987**, *42b*, 1291.

(14) *14.SHELXTL*, version. 5; Siemens Analytical X-ray Instruments Inc.: Madison, WI, 1994.

(15) Sheldrick, G. M. *SHELXL97*; University of Göttingen: Göttingen, Germany, 1997.

Table 1. Crystallographic Data for **1a**·2CH_3CN and **2**

	1a·2CH_3CN	**2**
empirical formula	$C_{56}H_{66}AsCrN_2OS_4$	$C_{30}H_{48}CrNOS_4$
fw	1038.27	618.93
space group	$P2_1/n$ (No. 14)	$P2_1/c$ (No. 14)
a (Å)	10.0423(6)	9.4339(4)
b (Å)	19.7433(12)	17.3904(7)
c (Å)	26.800(2)	19.6907(9)
β (deg)	96.93(2)	97.943(5)
V (Å)	5274.8(6)	3199.4(2)
Z	4	4
T (K)	100(2)	100(2)
ρ_{calcd} (g cm^{-3})	1.307	1.285
reflns collected/$2\Theta_{max}$	45009/50.00	60094/60.00
unique reflns/$I > 2\sigma(I)$	9203/7290	9325/6767
no. of params/restraints	613/6	342/6
λ (Å)/μ(Mo Kα) (cm^{-1})	0.71073/10.38	0.71073/6.42
R1[a]/GOF[b]	0.0982/1.202	0.0459/1.038
wR2[c] ($I > 2\sigma$ (I))	0.2040	0.0930
residual density (e Å^{-3})	+1.15/−0.66	+0.34/−0.40

[a] Observation criterion: $I > 2\sigma(I)$. $R1 = \sum||F_o| - |F_c||/\sum|F_o|$. [b] $GOF = [\sum[w(F_o^2 - F_c^2)^2]/(n - p)]^{1/2}$. [c] $wR2 = [\sum[w(F_o^2 - F_c^2)^2]/\sum[w(F_o^2)^2]]^{1/2}$, where $w = 1/\sigma^2(F_o^2) + (aP)^2 + bP$, $P = (F_o^2 + 2F_c^2)/3$.

of the ligands in compound **2** was found to be disordered over two sites. The distribution of C(7) in the first ligand and C(17) in the second is significantly different (~78:22 vs 55:45).

Physical Measurements. Electronic absorption spectra of the complexes and spectra from the spectroelectrochemical measurements were recorded on an HP 8452A diode array spectrophotometer (range of 200−1100 nm). Cyclic voltammograms and coulometric electrochemical experiments were performed with an EG&G potentiostat/galvanostat. Temperature-dependent (2−298 K) magnetization data were recorded with a SQUID magnetometer (MPMS Quantum Design) in an external magnetic field of 1 T. The experimental magnetic susceptibility data were corrected for underlying diamagnetism using tabulated Pascal's constants. X-band EPR spectra were recorded with a Bruker ESP 300 spectrometer. Magnetic circular dichroism spectra were obtained on a home-built instrument consisting of a JASCO J-715 spectropolarimeter and an Oxford Instruments SPECTROMAG magnetocryostat (generating magnetic fields of up to 11 T). Spectra were taken for samples dissolved in butyronitrile which gave high-quality glasses suitable for optical spectroscopy at cryogenic temperatures. Simultaneous Gaussian resolution of the absorption and MCD spectra was performed using the PeakFit 4 program, and the *C/D* ratios were calculated by

$$\frac{C}{D} = \frac{k_B T}{\mu_B B} \frac{\int \frac{\Delta\epsilon(\nu)}{\nu} d\nu}{\int \frac{\epsilon(\nu)}{\nu} d\nu}$$

for spectra taken in the linear region of the MCD C-term response (30.2 K and 5 T).

X-ray Absorption Spectroscopy. All data were measured at the Stanford Synchrotron Radiation Laboratory under ring conditions of 3.0 GeV and 60−100 mA.

Cr K-edge XAS data were measured on the unfocused bend magnet beam line 2-3 or the focused 16-pole wiggler beam line 9-3. A Si(220) monochromator was utilized for energy selection. The monochromator was detuned 50% (for beam line 2-3) to minimize higher harmonic components in the X-ray beam (for beam line 9-3, a harmonic rejection mirror was present). All samples were prepared as solids in boron nitride, pressed into a pellet and sealed between 38 μm Kapton tape windows in a 1 mm aluminum spacer. The temperature was maintained at 10 K during data collection using an Oxford Instruments CF1208 continuous-flow liquid helium cryostat. The data were measured in transmission mode. Internal energy calibrations were performed by simultaneous measurement of a Cr reference foil placed between the second and third ionization chamber. The first inflection point was assigned to 5989.0 eV. The data represent 3−5 scan averages and were processed by fitting a second-order polynomial to the preedge region and subtracting this background from the entire spectrum. A three-region cubic spline was used to model the smooth background above the edge. The data were normalized by subtracting the spline and normalizing the postedge to 1.0.

S K-edge data were measured using the 54-pole wiggler beam line 6-2 in a high-magnetic field mode of 10 kG with a Ni-coated harmonic rejection mirror and a fully tuned Si(111) double-crystal monochromator. Details of the optimization of this setup for low-energy studies have been described previously.[16] Data were measured at room temperature by fluorescence using a Lytle detector. To check for reproducibility, 2−3 scans were measured for each sample. The energy was calibrated from the S K-edge spectra of $Na_2S_2O_3 \cdot 5H_2O$, run at intervals between sample scans. The maximum of the first preedge feature in the spectrum was fixed at 2472.02 eV. A step size of 0.08 eV was used over the edge region. Data were averaged, and a smooth background was removed from all spectra by fitting a polynomial to the preedge region and subtracting this polynomial from the entire spectrum. Normalization of the data was accomplished by fitting a flattened polynomial or straight line to the postedge region (2490−2740 eV) and normalizing the postedge to 1.0.

Calculations. All calculations in this work were performed with the electronic structure program ORCA.[17] As will be further discussed in the text, the geometry optimizations were carried out at the BP86 level[18] of DFT. In analogy to the previous studies,[12d] in which dithiolene complexes with heavier metals were studied, the present calculations have been performed with inclusion of scalar relativistic effects at the second-order Douglas−Kroll−Hess level (DKH2).[19] In the geometry optimizations, the one-center approximation was used which eliminates DKH2 contributions to the analytic gradients. In the context of ZORA[20a], the one-center approximation has been shown to introduce only minor errors to the final geometries.[20b] Large uncontracted Gaussian basis sets, which were derived from the well-tempered basis sets of Huzinaga,[21] were used at the metal center. For the remaining atoms, the all-electron polarized triple-ξ (TZVP)[22] Gaussian basis sets of Ahlrich's group were used; they were further uncontracted to allow for a distortion of the inner-shell orbitals in the presence of the relativistic potential.

(16) Hedman, B.; Frank, P.; Gheller, S. F.; Roe, A. L.; Newton, W. E.; Hodgson, K. O. *J. Am. Chem. Soc.* **1988**, *110*, 3798.
(17) Neese, F. *ORCA, An Ab Initio, DFT, and Semiempirical Electronic Structure Package*, version 2.4, revision 16; Max-Planck Institut für Bioanorganische Chemie: Mülheim, Germany, 2004.
(18) (a) Becke, A. D. *J. Chem. Phys.* **1988**, *84*, 4524. (b) Perdew, J. P. *Phys. Rev. B* **1986**, *33*, 8522.
(19) Hess, B. A.; Marian, C. M. In *Computational Molecular Spectroscopy*; Jensen, P., Bunker, P. R., Eds.; John Wiley & Sons: New York, 2000; p 169 ff.
(20) (a) van Lenthe, E.; Snijders, J. G.; Baerends, E. J. *J. Chem. Phys.* **1996**, *105*, 6505. (b) van Lenthe, J. H.; Faas, S.; Snijders, J. G. *Chem. Phys. Lett.* **2000**, *328*, 107.
(21) (a) Huzinaga, S.; Miguel, B. *Chem. Phys. Lett.* **1990**, *175*, 289. (b) Huzinaga, S.; Klobukowski, M. *Chem. Phys. Lett.* **1993**, *212*, 260.
(22) (a) Schäfer, A.; Horn, H.; Ahlrichs, R. *J. Chem. Phys.* **1992**, *97*, 2571. (b) Schäfer, A.; Huber, C.; Ahlrichs, R. *J. Chem. Phys.* **1994**, *100*, 5289.

Table 2. Redox Potentials of the Complexes at 20 °C

complex	$E_{1/2}^1$ (V vs Fc^+/Fc)	$E_{1/2}^2$ (V vs Fc^+/Fc)
1[a]	+0.16 (quasi-reversible)	−0.96
2[a]	+0.15 (quasi-reversible)	−0.96
$[MoO(L)_2]^{1-}$[b]	*c*	−0.40

[a] CH_2Cl_2 solution. [b] Dimethyl formamide solution. [c] Experimental value not available.

The property calculations at the optimized geometries were done with the B3LYP functional.[23] In this case, the same basis sets were used but the quasirelativistic ZORA method[20] was used because, in this formalism, the magnetic properties are more readily formulated.[24] For the calculation of the EPR parameters, the Fermi contact and the dipolar and metal spin−orbit contributions are included. TD-DFT calculations were carried out according to ref 25. Large uncontracted Gaussian basis sets, derived from the well-tempered basis sets of Huzinga,[21] were also used at the sulfur atoms for the calculation of sulfur K-edge spectra. In the solution of the TD-DFT equations, only transitions from a single localized sulfur 1s orbital into all virtual levels were taken into account. Both the electric dipole and quadrupole contributions to the preedge intensity were considered in the calculation.

Results

Synthesis. The reaction of 3,5-di-*tert*-butyl-1,2-benzenedithiol, $H_2[L^{Bu}]$, and NEt_3 (1:2) with $CrCl_3(THF)_3$ in acetonitrile in the presence of oxygen yields the reddish-brown spin-doublet monoanion $[Cr^VO(L^{Bu})_2]^{1-}$. Microcrystalline deep-brown $[N(n\text{-}Bu)_4][Cr^VO(L^{Bu})_2]$ (**1**) was isolated in a 60% yield after addition of $[N(n\text{-}Bu)_4]Br$. In the infrared spectrum, the $\nu(Cr{=}O)$ stretch is observed at 967 cm^{-1}. With $[As(Ph)_4]Br$ used in the above reaction, the salt $[As(Ph)_4][CrO(L^{Bu})_2]\cdot 2CH_3CN$ (**1a**·$2CH_3CN$) was prepared, and single crystals suitable for X-ray crystallography were obtained.

Similarly the reaction of disodium (4-methyl-1,2-benzenedithiolate), Na_2L^{Me}, in MeOH with $CrCl_2$ (2:1) in the presence of oxygen yielded the $[Cr^VO(L^{Me})_2]^{1-}$ anion. After the addition of $[N(n\text{-}Bu)_4]Br$, the $[N(n\text{-}Bu)_4][Cr^VO(L^{Me})_2]$ (**2**) salt was obtained. Single crystals suitable for X-ray crystallography were obtained for **2** by recrystallization of the crude product from a THF solution at −20 °C. The $\nu(Cr{=}O)$ stretch is observed at 964 cm^{-1}.

Electro- and Spectroelectrochemistry. Cyclic voltammograms of complexes **1** and **2** have been recorded at 25 °C in CH_2Cl_2 solutions containing 0.10 M $[N(n\text{-}Bu)_4]PF_6$ as the supporting electrolyte. The redox potentials are referenced versus the ferrocenium/ferrocene (Fc^+/Fc) couple. Table 2 summarizes the results.

The CV of **2** (Figure 1) displays one fully reversible one-electron reduction at −0.96 V and a quasireversible one-electron oxidation at +0.150 V. A comparison of these data with those reported for the corresponding $[MoO(L)_2]^{1-}$ complex[10a] shows that the one-electron reduction processes at −0.96 V for **2** and at −0.40 V for $[MoO(L)_2]^{1-}$ are highly dependent on the nature of the central metal ion involved. This is consistent with an essentially metal-centered reduction (eq 1).

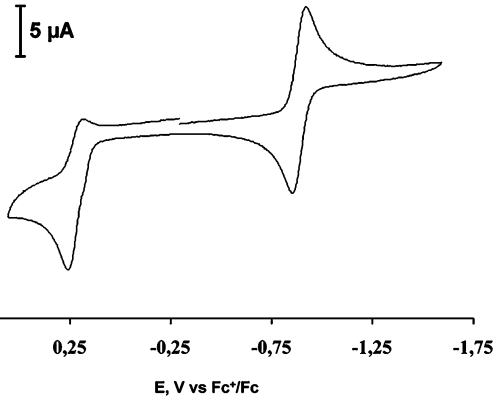

Figure 1. Cyclic voltammogram of **2** in CH_2Cl_2 solution containing 0.10 M $[(n\text{-}Bu)_4N]PF_6$ as the supporting electrolyte at a scan rate of 200 mV s^{-1} at 25 °C (glassy carbon electrode, potentials referenced vs the ferrocenium/ferrocene couple).

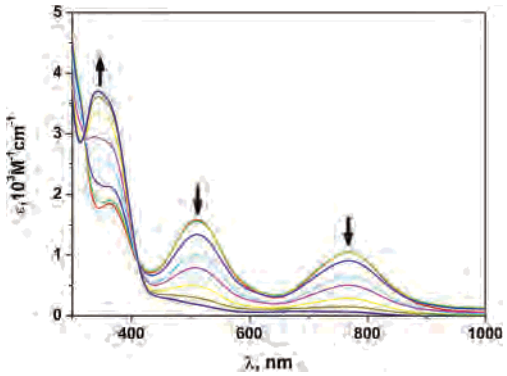

Figure 2. Spectral changes associated with the one-electron coulometric reduction of **2** in CH_2Cl_2 solution (0.10 M $[N(n\text{-}Bu)_4]PF_6$) at −25 °C.

$$[M^VO(L)_2]^{1-} \underset{-e}{\overset{+e}{\rightleftharpoons}} [M^{IV}O(L)_2]^{2-} \qquad (1)$$

Because the one-electron reduced form of **2** is stable in CH_2Cl_2 solution, its electronic spectrum was recorded. In contrast, the one-electron oxidized species decomposed during the coulometric process. Figure 2 exhibits the spectrum of **2** together with the spectral changes associated with its one-electron electrochemical reduction. The absorption spectrum of **2** features two moderately intense low-energy transitions at 770 and 515 nm, both of which disappear in the reduced species ($\mathbf{2}^{red}$). A combination of MCD and electronic structure calculations has been used below to understand the origin of these low-energy transitions in **2**. It is important to note that both **2** and $\mathbf{2}^{red}$ lack any intense ($>10^4$ M^{-1} cm^{-1}) intervalence ligand-to-ligand charge transfer transition in the near-infrared region, which has been previously established as a marker band[12] for the presence of dithiobenzosemiquinonate(1−) radicals in planar bis(dithiolene) coordination complexes. This is furthur evidence against the possibility of the presence of any ligand-based redox chemistry for the $[CrO(L^{Me})_2]^{2-/1-}$ couple. The absorption spectrum of **1** is very similar to that of **2** (Table 3).

(23) (a) Lee, C.; Yang, W.; Parr, R. G. *Phys. Rev. B* **1988**, *37*, 785. (b) Becke, A. D. J. *Chem. Phys.* **1993**, *98*, 5648.
(24) van Lenthe E.; van der Avoird, A.; Wormer, P. E. S. *J. Chem. Phys.* **1998**, *108*, 4783.
(25) Neese, F.; Olbrich, G. *Chem. Phys. Lett.* **2002**, *362*, 170.

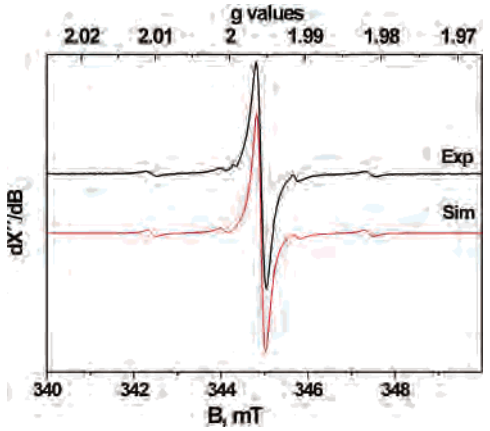

Figure 3. X-band EPR spectrum of **1** in CH_2Cl_2 solution at 25 °C (frequency = 9.6355 GHz, modulation = 10.0 G, power = 504 μW). For simulation parameters (W_x = 15, W_y = 15, W_z = 15 Hz), see text.

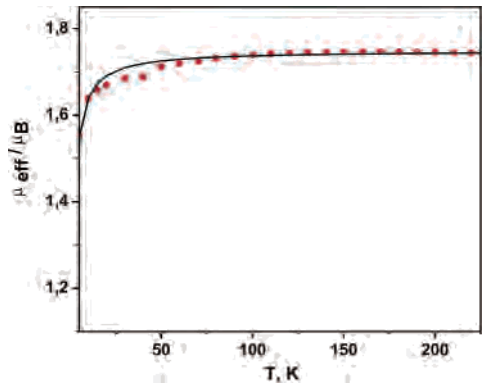

Figure 4. Temperature dependence of the effective magnetic moment, μ_{eff}, of **1** in an external applied field of 1 T.

Table 3. Electronic Spectra of Complexes in CH_2Cl_2 Solutions

complex	T (°C)	λ_{max} (nm) (ϵ ($\times 10^4$ M^{-1} cm^{-1}))
1	20	385(0.18), 498(0.16), 731(0.10)
2	20	382(0.19), 515(0.17), 770(0.11)
$\mathbf{2}^{red}$	−25	378(0.36)

Magnetic Properties and EPR Spectra. The room-temperature (298 K) EPR spectrum of **1** in CH_2Cl_2 solution (Figure 3) displays a sharp isotropic signal (g_{iso} = 1.996) with hyperfine interaction from the ^{53}Cr (I = 3/2) nucleus (A_{iso} = 35 MHz). The magnetic anisotropy in the g tensors (g_x = 1.98, g_y = 1.99, and g_z = 2.02) obtained from the simulation of the frozen CH_2Cl_2 solution X-band EPR spectra of **1** at 10 K (Figure S2) are found to be typical of other Cr(V) oxo complexes with sulfur donor ligands.[8b,11] However, the anisotropy in the ^{53}Cr hyperfine splitting is not resolved within the line width (30 G) of the experiment.

The magnetization curve of **1** (Figure 4) displays an effective magnetic moment of 1.7 μ_B in the region of 100−225 K. This value corresponds to the expected spin-only value for an S = 1/2 ground state. The best fit (solid line in the Figure 4) of the experimental data resulted in the following fit-parameters: g_{Cr} = 1.996, χ_{TIP} = 0.38 × 10^{-3} emu, and θ = −4.20 K, where the g value is fixed from the EPR analysis.

Cr K-Edge XAS. Metal K-edge X-ray absorption spectroscopy (XAS) is a powerful local probe of the geometric and electronic structure of the central metal ion in coordination complexes. The XAS edge is sensitive to the electronic structure and may be used as an indicator of the oxidation state.[26] The preedge region (resulting from electric dipole forbidden 1s → 3d transitions) is particularly diagnostic and an increase in the preedge energy can be correlated to an increase in the oxidation state of the central metal ion. In addition, the preedge region provides a measure of 3d−4p mixing and thus increased intensity may be induced by exceptionally short metal−ligand bonds.[26]

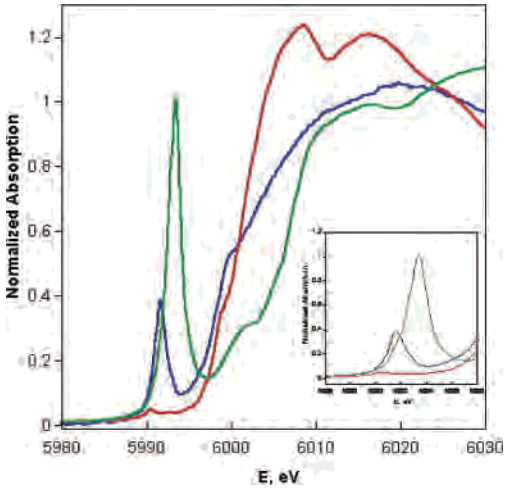

Figure 5. Normalized Cr K-edge X-ray absorption spectra of **1** (blue), K_2CrO_4 (green), and *trans*-$[Cr(H_2O)_4Cl_2]Cl$ (red). The inset is an expansion of the preedge region.

Figure 5 compares the Cr K-edge spectrum of **1** with that of known Cr(III) and Cr(VI) complexes. Because of the presence of two-electron ligand-to-metal charge-transfer transitions in the ∼5995−6005 eV range, the rising edge regions are difficult to compare. However, the preedge can be used as an indication of the oxidation state trends. The preedge energy of **1** at 5991.75 eV is ∼2 eV higher than in *trans*-$[Cr(H_2O)_4Cl_2]Cl$ (at 5989.6 eV) and ∼1 eV lower than in K_2CrO_4 (5992 eV). Since an increase of ∼1 eV per oxidation state is typical for first-row transition metals, the present XAS data supports the Cr(V) assignment for **1**. The preedge intensity of **1** is intermediate between that of O_h *trans*-$[Cr(H_2O)_4Cl_2]Cl$ and T_d K_2CrO_4, and this indicates significant metal 3d−4p mixing in **1** which likely comes from the short Cr(V)−oxo bond.

S K-Edge XAS. The sulfur K-edge results from an electric dipole-allowed local 1s → 4p transition.[27] In cases where the ligand is bound to a transition metal with a partially filled d shell, the covalent interaction between the ligand 3p orbitals and the metal 3d orbitals produces partial-ligand 3p hole character, resulting in a preedge transition, the intensity of which will reflect the covalency of the metal−ligand

(26) DuBois, J. L.; Mukherjee, P.; Stack, T. D. P.; Hedman, B.; Solomon, E. I.; Hodgson, K. O. *J. Am. Chem. Soc.* **2000**, *122*, 5775. (b) Westre, T. E.; Kennepohl, P.; DeWitt, J. G.; Hedman, B.; Hodgson, K. O.; Solomon, E. I. *J. Am. Chem. Soc.* **1997**, *119*, 6297.

(27) (a) Glaser, T.; Hedman, B.; Hodgson, K. O.; Solomon, E. I. *Acc. Chem. Res.* **2000**, *33*, 859. (b) Solomon, E. I.; Hedman, B.; Hodgson, K. O.; Dey, A.; Szilagyi, R. K. *Coord. Chem. Rev.* **2005**, *249*, 97.

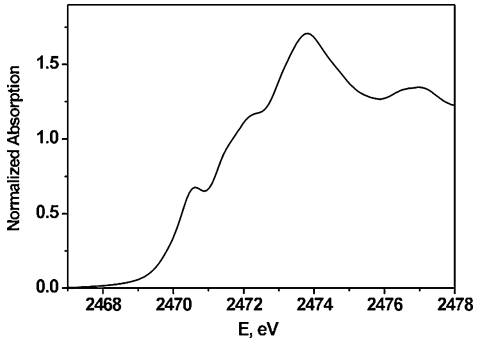

Figure 6. Normalized sulfur K-edge spectrum of solid **1**.

bond.[27,28] Furthermore the energy of the preedge transition is affected by the energy of the unoccupied (or partially occupied) 3d orbitals (which will have contributions from the ligand field and effective nuclear charge (Z_{eff})) and the energy of the ligand 1s core.

The sulfur K-edge XAS spectrum of **1** is shown in Figure 6. In the preedge region (2468−2471 eV) it exhibits a broad preedge feature centered at ∼2470.5 eV. To interpret this as a single preedge transition, it would be necessary to consider an unusually large bandwidth of ∼1.5 eV. On the basis of the DFT calculations presented below, it will be argued that the broad preedge feature in Figure 6 may actually result from the superposition of five individual preedge transitions (see Figure 11 below). The higher energy features in Figure 6 are typical of complexes having thiophenolate ligands[29] and are best assigned as "rising" edge features because of a sulfur 1s to C−S σ^* transition followed by transitions into the sulfur 4p levels and finally into the continuum.

X-ray Crystallography. The crystal structures of **1a**·$2CH_3CN$ and **2** have been determined at 100 K. The structure of the anions in **1a**·$2CH_3CN$ (top) and **2** (bottom) are shown in Figure 7. Crystallographic details are given in Table 1. Table 4 summarizes the important bond distances and dihedral angles.

The coordination environment around the Cr in both **1a** and **2** is approximately square-based pyramidal. The Cr atom is displaced above the square plane defined by the four sulfur atoms by 0.720 Å in **1a** and by 0.694 Å in **2**. A structural feature of interest in both complexes is the dihedral angle, φ (see Figure 7), between the mean S−C−C−S trapezoidal plane and the Cr−S−S plane which results in the bending of the dithiolate ligand about the S−S vector. In both complexes, the extent of this folding about the Cr atom is different for each of the ligands. In **1a**, the angle is 141.7° (angle φ1 is X(1E)−X(1B)−Cr(1) in Figure 7) on one side and 163.4° (angle φ2 is X(1D)−X(1C)−Cr(1) in Figure 7) on the other. In **2**, while the S(12)C(12)C(11)S(11) trapezoidal plane is almost coplanar (φ2 = 175.1°) with the Cr(1)S(12)S(11) plane, the S(2)C(2)C(1)S(1) plane makes an angle (φ1) of 155.3° with the Cr(1)S(2)S(1) plane. Interestingly, the dihedral angles, φ, on either side of the chromium atom differ by ∼20° ($\Delta\varphi = \varphi 2 - \varphi 1$) for both complexes. On the basis of the DFT calculations presented below, it will be argued that the above distortion is not the result of crystal packing effects, but it is electronic in origin.

The observed Cr−O bond distances of 1.572(7) and 1.5796(15) Å in **1a** and **2**, respectively, are similar to other known Cr^{V}═O bonds.[5,6,30] The average Cr−S distances in **1a** (2.271(3) Å) and **2**(2.2832(6) Å) are slightly shorter than

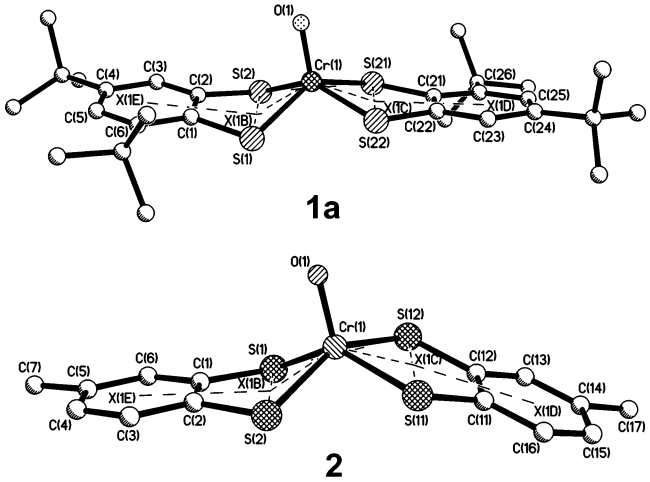

Figure 7. Structure of the monoanions in crystals of **1a**·$2CH_3CN$ (top) and **2** (bottom). For **1a** the points X1B and X1C represent the centroids of S(1), S(2) and S(21), S(22), respectively. Similarly, the points X(1D) and X(1E) represent the centroids of C(21)−C(26) and C(1)−C(6), respectively. The dihedral angles, φ1 and φ2, are defined by the angles X1E−X1B−Cr(1) and X1D−X1C−Cr(1), respectively. φ1 and φ2 are defined in the same way for complex **2**.

Table 4. Selected Bond Distances (Å) and Dihedral Angles in **1a** and **2**

		1a	
Cr(1)−O(1)	1.572(7)	Cr(1)−S(21)	2.267(2)
Cr(1)−S(1)	2.278(3)	Cr(1)−S(22)	2.274(2)
Cr(1)−S(2)	2.276(3)	S(21)−C(21)	1.759(8)
S(1)−C(1)	1.787(8)	S(22)−C(22)	1.758(8)
S(2)−C(2)	1.785(8)	C(21)−C(22)	1.42(1)
C(1)−C(2)	1.42(1)	C(21)−C(26)	1.41(1)
C(1)−C(6)	1.40(1)	C(22)−C(23)	1.39(1)
C(2)−C(3)	1.40(1)	C(23)−C(24)	1.38(1)
C(3)−C(4)	1.38(1)	C(24)−C(25)	1.39(1)
C(4)−C(5)	1.40(1)	C(25)−C(26)	1.41(1)
C(5)−C(6)	1.39(1)		
φ1	141.7°	φ2	163.4°
		2	
Cr(1)−O(1)	1.5796(15)	Cr(1)−S(11)	2.2878(6)
Cr(1)−S(1)	2.2689(6)	Cr(1)−S(12)	2.2869(6)
Cr(1)−S(2)	2.2895(6)	S(11)−C(11)	1.755(2)
S(1)−C(1)	1.763(2)	C(12)−S(12)	1.748(2)
S(2)−C(2)	1.758(2)	C(11)−C(12)	1.397(3)
C(1)−C(2)	1.401(3)	C(11)−C(16)	1.397(3)
C(1)−C(6)	1.399(3)	C(12)−C(13)	1.406(3)
C(3)−C(2)	1.399(3)	C(13)−C(14)	1.379(4)
C(3)−C(4)	1.383(3)	C(14)−C(15)	1.400(4)
C(4)−C(5)	1.386(3)	C(15)−C(16)	1.387(3)
C(5)−C(6)	1.392(3)		
φ1	155.3°	φ2	175.1°

(28) Neese, F.; Hedman, B.; Hodgson, K. O.; Solomon, E. I. *Inorg. Chem.* **1999**, *38*, 4854.
(29) (a) Glaser, T.; Rose, K.; Shadle, S. E.; Hedman, B.; Hodgson, K. O.; Solomon, E. I. *J. Am. Chem. Soc.* **2001**, *123*, 442. (b) Dey, A.; Glaser, T.; Couture, M. M.-J.; Eltis, L. D.; Holm, R. H.; Hedman, B.; Hodgson, K. O.; Solomon, E. I. *J. Am. Chem. Soc.* **2004**, *126*, 8320.
(30) Krumpolc, M.; DeBoer, B. G.; Rocek, J. *J. Am. Chem. Soc.* **1978**, *100*, 145.

Table 5. Calculated and Experimental (in parentheses) Bond Lengths (Å) and Dihedral Angles (deg) in $[CrO(L)_2]^{1-}$ and $[CrO(L)_2]^{2-}$ as Obtained from the Scalar Relativistic ZORA BP86 DFT Calculations Using Large Uncontracted Gaussian Basis Sets at the Metal and Uncontracted All-Electron Polarized Triple-ξ (TZVP) Gaussian Basis Sets for the Remaining Atoms

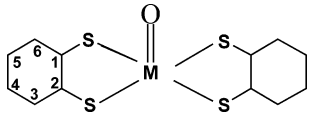

	$[CrO(L)_2]^{1-}$	$[CrO(L)_2]^{2-}$
Cr−S	2.308 (2.2832(6))[a]	2.311
Cr−O	1.580 (1.5796(15))	1.610
C−S	1.769 (1.760(2))	1.770
C_1-C_2	1.401 (1.401(3))	1.408
C_2-C_3	1.394 (1.399(3))	1.395
C_3-C_4	1.392 (1.383(3))	1.396
C_4-C_5	1.398 (1.386(3))	1.390
Φ1	156.2 (155.3)	178.9
Φ2	178.8 (175.1)	178.3

[a] Experimental bond length for **2**.

the Cr−S bond distances (2.30 Å) obtained from the EXAFS analysis on a series of chromium(V) glutathione complexes.[8b] The six C−C distances of the phenyl ring are equidistant in **1a** and **2** within the experimental error (±0.02 Å for **1a** and ±0.01 Å for **2**, 3σ). The average C−C distances of 1.393 (**1a**) and 1.398 Å (**2**) are typical for aromatic phenyl rings. In particular, the C−S bonds with average lengths of 1.786 ± 0.02 (**1a**) and 1.762 ± 0.01 Å (**2**) are long and indicate the presence of S,S-coordinated aromatic 1,2-dithiolate ligands. Once more, this supports the Cr(V) assignment for the complexes.

Calculations

In this section a detailed picture of the electronic structure of the monoanionic complex $[Cr(L)_2O]^{1-}$ is derived from DFT calculations, where L represents the unsubstituted dianion benzene-1,2-dithiolate.

Calculated Geometries. The calculated geometry and metrical parameters for the $[Cr(L)_2O]^{1-}$ species are found to be in good agreement with the experimental values (Table 5). The approximate square-based pyramidal geometry is well-reproduced in the calculation. Moreover, symmetry lowering from C_{2v} to C_s because of the folding of the C−S−S−C trapezoid along the S−S vector on either side of the Cr atom is observed, which is in agreement with the experimental observations. The dihedral angles of the two ligands are nicely reproduced in the calculation with errors of <5° (compared to **2**). The presence of the terminal oxo donor results in the metal residing ~0.62 Å (calculated 0.67 Å) out of the bis(dithiolene) S_4 plane, providing considerably less S(p)−Cr(d) π-orbital overlap than the previously reported square planar transition metal bis(dithiolenes).[12] The experimental distortion, nicely reproduced by the calculations, is thus, electronic in origin.

To further understand the basis of the C_{2v} to C_s distortion in the $[Cr(L)_2O]^{1-}$ anion, DFT calculations have been performed on both the C_{2v} and C_s models. The reason for the distortion is most clearly revealed by the C_s bonding

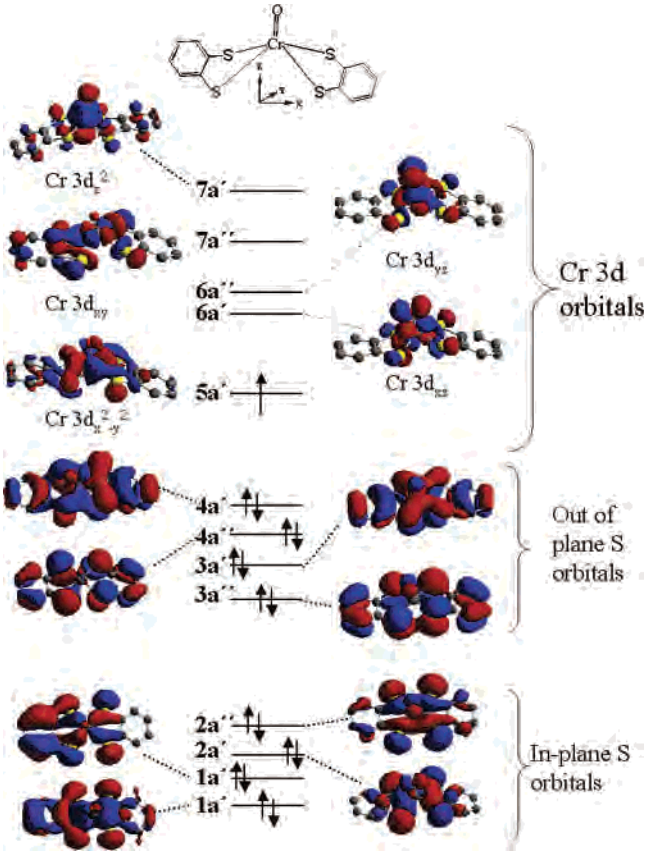

Figure 8. Kohn−Sham MOs and the energy scheme of the $[CrO(L)_2]^{1-}$ anion as obtained from a spin-unrestricted ZORA B3LYP DFT calculation.

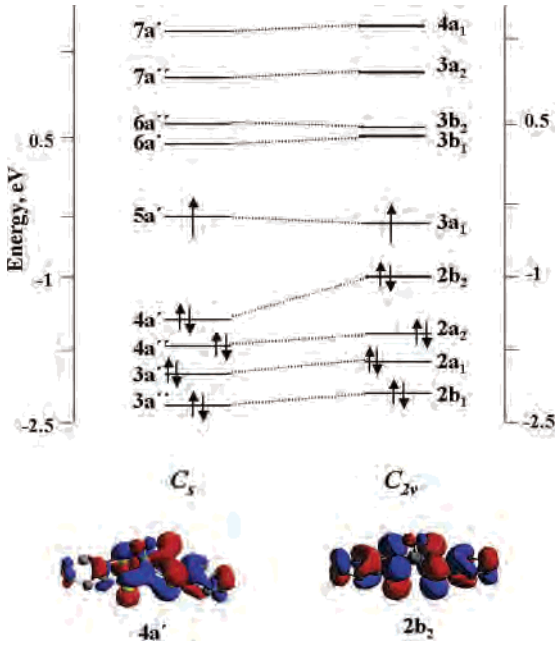

Figure 9. Orbital-correlation diagram for the $[CrO(L)_2]^{1-}$ anion illustrating the changes in energy of the selected molecular orbitals on moving from C_{2v} to C_s symmetry.

scheme shown in Figure 8 and the orbital correlation diagram in Figure 9. The C_s model is found to be more stable by 4.8 kcal/mol. On going from the C_{2v} to C_s geometry, the 4a′ π-type orbital (see Figure 9) is found to be appreciably stabilized (5.3 kcal/mol). This increased stabilization is the

result of a better overlap, and consequently better π-donation, of the filled sulfur p_z orbitals with the singly occupied in-plane Cr($3d_{x^2-y^2}$) orbital (4a′ orbital in Figure 9). In the C_{2v} model, the sulfur p_z orbitals ($2b_2$ orbital in Figure 9) are almost orthogonal to the Cr($3d_{x^2-y^2}$) orbital, and the stabilizing Cr(d)−S(p) π-interaction is absent. Thus, the C_s structure is favored in comparison to the C_{2v} structure mainly bcause of the stabilization energy of the 4a′ orbital in the distorted form. Similar distortions leading to increased stabilizing interactions of the filled symmetric sulfur p_π interactions have been reported previously in the molybdenum and tungsten oxotransferases.[31]

While the distortion of one ligand leads to the stabilization described above, an equivalent distortion in both ligands, leading to same angle φ on each side of the Cr atom, will have a destabilizing effect. Thus, it is intuitively appealing that the twisting of the two ligands on both sides of the Cr will be interrelated to each other; a stronger interaction on one side will lead to a weaker interaction on the other and vice versa. The similar $\Delta\varphi$ values of ∼20° for both the complexes, thus represent a compromise in the orientation of the two ligands required to satisfy the π-acidity of the Cr(V) ion. In the calculation, this is predicted to be 22°, in good agreement with the experimental value.

The one-electron reduction of the $[Cr(L)_2O]^{1-}$ anion results in the double occupancy of the Cr($3d_{x^2-y^2}$) orbital. Consequently, the Cr($3d_{x^2-y^2}$) ↔ S(p) π-interaction will now have a destabilizing effect. Thus the ligands will orient themselves to minimize this repulsive interaction. Thus the calculated geometry of the $[Cr(L)_2O]^{2-}$ species is approximately C_{2v}. In contrast to the $[Cr(L)_2O]^{1-}$ species, the calculated dihedral angles, φ, for both the ligands in $[Cr(L)_2O]^{2-}$ are found to be ∼180° (Table 5). Although the experimental data for the chromium complex are not available for comparison, a crystal structure of the corresponding $[Mo(L)_2O]^{2-}$ dianion[10a] has been reported and is known to possess a C_{2v} geometry.

Bonding Scheme. For the MO description of the $[Cr(L)_2O]^{1-}$ complex within the C_s point group, the coordinate axes shown in Figure 8 were used. The qualitative bonding scheme derived from the B3LYP DFT calculation on the $[Cr(L)_2O]^{1-}$ complex is given in Figure 8.

In a series of previous publications,[17,26] it was shown that the concept of metal versus ligand oxidation in coordination complexes is controlled mainly by the relative energies of the metal *n*d and the sulfur 3p orbitals which in turn are controlled by a combination of the effective nuclear charge (Z_{eff}) and scalar relativistic effects of the central metal ion. Thus, the predominant ligand-based oxidation was observed for the $[Au(L)_2]^{1-/0}$ couple,[12a] and metal-based oxidation was observed for the $[Fe(L)_2]^{2-/1-}$ couple.[12c] The Cr(II) ion has a lower effective nuclear charge than Fe(II),[32] and hence, metal-based redox processes are expected to be predominant in the chemistry of the chromium dithiolene complexes. This

Table 6. Percentage Composition of the Selected Orbitals of the $[CrO(L)_2]^{1-}$ Anion as Obtained from the Scalar Relativistic ZORA B3LYP DFT Calculation Using Large Uncontracted Gaussian Basis Sets at the Metal and Uncontracted All-Electron Polarized Triple-ξ (TZVP) Gaussian Basis Sets for the Remaining Atoms

	Cr					S			O		
	$3d_{x^2-y^2}$	$3d_{xz}$	$3d_{yz}$	$3d_{xy}$	$3d_{z^2}$	$3p_x$	$3p_y$	$3p_z$	$2p_x$	$2p_y$	$2p_z$
4a′	20.1							44		4.0	
5a′	79.2							4.8		1.1	
6a′		60.1				4.8	4.9		20.6		
6a″			58.2			4.9	5.1			21.4	
7a″				45.5		19.3	15.2				
7a′					36.2			6.1			18.8

is indeed found to be the case, as is evident from the bonding scheme of the $[Cr(L)_2O]^{1-}$ complex shown in Figure 8. The Cr 3d orbitals are all placed at energies much higher than the ligand orbitals. The electronic configuration for Cr in $[Cr(L)_2O]^{1-}$ is formally $3d^1$, and this unpaired electron resides in the Cr($3d_{x^2-y^2}$)orbital, which is essentially metal−ligand nonbonding, leading to a doublet ground state. The other four d orbitals remain unoccupied. The d-orbital splitting, as shown in Figure 8, is thus predicted to be $3d_{x^2-y^2} < 3d_{xz}$,-$3d_{yz} < 3d_{xy} < 3d_{z^2}$. This splitting results from the fact that the terminal oxo ligand is an extremely strong σ- and π-donor, and in the presence of a moderate-to-weak equatorial ligand field, as in the present case, the d-orbital splitting diagram in Figure 8 results. The $3d_{z^2}$ and $3d_{xz}$,$3d_{yz}$ orbitals are strongly destabilized by σ- and π-antibonding interactions with the terminal oxo ligand to such an extent that they always tend to remain unoccupied. Beneath this d orbital manifold there is a set of eight orbitals corresponding to the symmetry-adapted linear combinations of the sulfur ligand 3p lone pairs (Figure 8). Four of the sulfur 3p orbitals in Figure 8 are in π-symmetry with respect to the Cr center. The remaining four possess σ-symmetry with respect to the metal.

The compositions of the selected orbitals in $[Cr(L)_2O]^{1-}$ are summarized in Table 6. The M−S covalency within the d orbital manifold is found to be significantly less in $[CrO(L)_2]^{1-}$ than that reported for the corresponding $[MoO(edt)_2]^{1-}$ anion (edt = ethane-1,2-dithiolate).[10b] Thus, the total sulfur p character for the 6a′(d_{xz}) and 6a″(d_{yz}) in $[CrO(L)_2]^{1-}$ is calculated to be ∼10%, compared to ∼22% in $[MoO(edt)_2]^{1-}$. Moreover, the 5a′ (79% $3d_{x^2-y^2}$) orbital in $[CrO(L)_2]^{1-}$ is also less covalent than the corresponding $10a_1$ orbital[34] calculated for $[MoO(L)_2]^{1-}$, which is 70% Mo $4d_{x^2-y^2}$. These covalency differences in the lowest-lying acceptor orbitals for the two compounds derive from the higher effective nuclear charge of Mo(V) compared to that of Cr(V). The Cr(V) d orbitals are placed at a higher energy with respect to the ligand orbitals, and the mixing of ligand and metal orbitals in $[CrO(L)_2]^{1-}$ is thus minimum.

The spin distribution in the$[Cr(L)_2O]^{1-}$ complex as obtained from the DFT calculation shows that almost the whole of the spin population (0.95) is localized on the Cr (Table S1). A significant negative spin population of −0.08

(31) Enemark, J. H.; Cooney, J. A.; Wang, J.-J.; Holm, R. H. *Chem. Rev.* **2004**, *104*, 1175.
(32) Gorelski, S. I.; Basumallick, L.; Vura-Weis, J.; Sarangi, R.; Hodgson, K. O.; Hedman, B.; Fujisawa, K.; Solomon, E. I. *Inorg. Chem.* **2005**, *44*, 4947.
(33) Earnshaw A. *Introduction to Magnetochemistry*; Academic Press: London, 1968.
(34) Neese F.; Solomon, E. I. *Inorg. Chem.* **1999**, *38*, 1847.

Table 7. Experimental and Calculated EPR Parameters for **1** Obtained from the Scalar Relativistic ZORA B3LYP DFT Calculation Using Large Uncontracted Gaussian Basis Sets at the Metal and Uncontracted All-Electron Polarized Triple-ξ (TZVP) Gaussian Basis Sets for the Remaining Atoms

	g_x	g_y	g_z	g_{iso}	A_{xx} MHz	A_{yy} MHz	A_{zz} MHz	A_{iso} MHz
calcd	1.978	1.986	2.015	1.993	8	5.4	78.3	23.1
exptl	1.98	1.99	2.02	1.996	*a*	*a*	*a*	35

[a] Magnetic anisotropy in the hyperfine splitting not resolved in the experimental spectrum.

(Table S1) is predicted in the calculation on the terminal oxygen atom. Indeed, a negative spin density on the terminal oxygen atom in $[Mo^{17}O(SPh)_4]^-$ has been suggested recently[10e] on the basis of the experimentally measured hyperfine and nuclear quadrupole interaction parameters for the oxo-^{17}O ligand. As explained in ref 10e, this negative spin density on the oxo ligand may originate from spin-polarization mechanisms.

Calculation of Properties. EPR Spectrum. The calculated EPR parameters are found to be in reasonably good agreement with experiment (Table 7). The predicted *g* tensor correctly reproduces the experimental finding that one principal *g* value (g_z) is larger than the free-electron *g* value, while the two perpendicular components are below it. This is unusual for a d^1 system, where all ligand-field excited states only contribute to negative shifts.[33] However, this observation is true for all thiolate-ligated transition metal (d^1) complexes[8b,11] and comes from the contributions of low-lying ligand-to-metal charge-transfer excitations (see below) in addition to the ligand-field excitations.

Excited-State Calculations. The room-temperature absorption and low temperature (5 K) MCD spectra of $[CrO(L^{Bu})_2]^{1-}$ have been subjected to Gaussian deconvolution in the range of 24 000−10 000 cm^{-1} to detect the individual transitions (Figure 10). As is commonly observed, the bands show a slight shift on going from ambient to liquid helium temperature, and therefore, equal band positions have not been enforced in the fit. The minimum number of Gaussian bands used was consistent with the experimentally observed peaks and shoulders, yielding a total of seven detectable transitions for **1** below 24 000 cm^{-1}.

The low symmetry of $[CrO(L)_2]^{1-}$ makes all transitions from the eight doubly occupied MOs in Figure 8 into the singly occupied 5a′($3d_{x^2-y^2}$) orbital and the four virtual d-based orbitals dipole allowed. These transitions are unipolarized, and spin−orbit coupling (SOC) to other states with noncollinear transition moments is required to obtain nonzero MCD intensity.[34] Both the SOC of the ground state with other states of same parity and the electric dipole-allowed excited states with states of same symmetry can contribute to the observed MCD signs. This excited-state SOC mechanism is also operative in addition to the ground-state SOC mechanism, since the spectrum is not strongly dominated by bands of only one sign, which is often the case if the ground-state SOC dominates the MCD response.[12c] The temperature dependence of the MCD spectrum (Figure S3) indicates that all the observed features result from a C-term mechanism

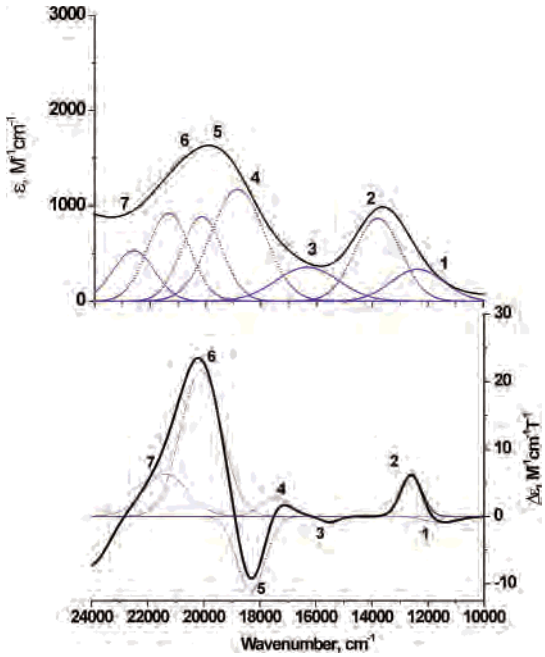

Figure 10. Deconvoluted room-temperature electronic absorption spectrum of **1** (top) and its magnetic circular dichroism (MCD) spectrum (bottom) recorded at 5 K and 5.0 T.

which is expected to dominate for paramagnetic molecules studied at low temperature.

Time-dependent DFT calculations (using the B3LYP functional, quasirelativistic ZORA method, and large uncontracted Gaussian basis sets as described in the Experimental Section) have been performed for the $[CrO(L)_2]^{1-}$ species. Four states with reasonable intensities are calculated in the range of 24 000−10 000 cm^{-1}, which is consistent with the four bands (bands 1 to 4) resolved in the simultaneous fit of the MCD and absorption spectra. These correspond to the LMCT transitions from the four out-of-plane sulfur p orbitals of π-symmetry to the singly occupied Cr $3d_{x^2-y^2}$ orbital. In the calculation, the lowest-energy band corresponds to the 4a′(S_π) → 5a′($3d_{x^2-y^2}$) transition. This transition is calculated at 12 500 cm^{-1} and is in good agreement with the experimentally observed transition (band 1 at 12 352 cm^{-1}). According to the MCD sign conventions established[10c] for transitions in C_s symmetry, a positive MCD band is expected for transitions involving a change in symmetry (a″→a′) and a negative MCD band is expected for transitions between states of the same symmetry (a′ → a′). Thus, a negative MCD sign for band 1 is expected and observed. The second transition calculated in the region of band 2 (positive MCD) is assigned as the 4a″(S_π) → 5a′ transition at 13 005 cm^{-1} with a calculated oscillator strength of 0.003. This is also in good agreement with the experimentally observed transition energy (13 790 cm^{-1}) and oscillator strength (0.008). The next transition is calculated at 16 500 cm^{-1} with an oscillator strength of 0.001. Its calculated symmetry is ^{2}A′ (3a′ → 5a′), and it is assigned to band 3, which is observed at 16 358 cm^{-1}. The observed MCD sign is negative because it corresponds to a transition between states of the same symmetry. The final LMCT transition below 23 000 cm^{-1} is calculated in the region of

Table 8. Analysis of the Optical Transitions for $[CrO(L)_2]^{1-}$ Following Gaussian Deconvolution of the ABS and MCD Spectra Shown in Figure 10 Combined with the Results of the Time-Dependent Density Functional Calculations at the Scalar Relativistic ZORA B3LYP Level

	energy (cm^{-1})			oscillator strength			
band	exptl	calcd	method	exptl	calcd	*C/D*	assignment
1	12 352	12 500	abs	0.003	0.001		$^2A'$ ($4a' \rightarrow 5a'(d_{x^2-y^2})$)
	11 609		MCD			−0.003	
2	13 790	13 005	abs	0.008	0.003		$^2A''$ ($4a'' \rightarrow 5a'(d_{x^2-y^2})$)
	12 585		MCD			+0.02	
3	16 358	16 500	abs	0.004	0.001		$^2A'$ ($3a' \rightarrow 5a'(d_{x^2-y^2})$)
	15 548		MCD			−0.001	
4	18 874	17 550	abs	0.012	0.04		$^2A''$ ($3a'' \rightarrow 5a'(d_{x^2-y^2})$)
	17 436		MCD			+0.003	
5	20 157	21 000	abs	0.007	0.001		$^2A'$ ($5a'(d_{x^2-y^2}) \rightarrow 6a'(d_{xz})$)
	18 336		MCD			−0.40	
6	21 339	22 345	abs	0.008	0.002		$^2A''$ ($5a'(d_{x^2-y^2}) \rightarrow 6a''(d_{yz})$)
	20 082		MCD			+0.67	
7	22 649	23 800	abs	0.004	0.001		$^2A''$ ($5a'(d_{x^2-y^2}) \rightarrow 7a''(d_{xy})$)
	21 390		MCD			+0.33	

the most intense band (band 4) at 17 550 cm^{-1} (experimental 18 874 cm^{-1}) with an oscillator strength of 0.02, and it corresponds to the transition $3a''(S_\pi) \rightarrow 5a'$. Band 4 corresponds to a positive MCD as expected.

Bands 5 (20 157 cm^{-1}) and 6 (21 339 cm^{-1}) constitute the negative and positive components of a positive pseudo-A term in the MCD spectrum of $[CrO(L^{Bu})_2]^{1-}$. High *C/D* ratios (Table 8) and pseudo-A behavior identify these as $3d_{x^2-y^2} \rightarrow 3d_{xz,yz}$ transitions, the degeneracy of the $3d_{xz,yz}$ orbitals being lifted by the C_s symmetry of the molecule. The negative sign of the lower-energy MCD component (band 5) indicates that $3d_{xz}$ lies lower in energy than $3d_{yz}$, in agreement with the bonding scheme shown in Figure 8. The next feature, toward higher energy, is a positive MCD peak (band 7) at 22 649 cm^{-1} which is just inside the tail of the increasing absorbance intensity. This positive MCD feature is reasonably assigned as the $5a'(3d_{x^2-y^2}) \rightarrow 7a''(3d_{xy})$ transition on the basis of its high *C/D* ratio. TD-DFT calculations also reproduce the above trend of the ligand-field transitions in $[CrO(L)_2]^{1-}$ (Table 8).

The one-electron reduction of $[CrO(L)_2]^{1-}$ puts the excess electron in the Cr $3d_{x^2-y^2}$ orbital. Thus, the low-energy LMCT transitions to the doubly occupied Cr $3d_{x^2-y^2}$ orbital are no longer possible in $[CrO(L)_2]^{2-}$. No transitions with significant intensities are calculated among the first 25 states (5500−25 000), in agreement with the experimental data.

S K-Edge XAS Calculations. From the S K-edge spectrum of **1**, which reveals a broad preedge feature at ~2470.5 eV, the number of preedge transitions cannot be unambiguously determined. Moreover, consideration of a single transition in the preedge region leads to an unusually large line width of 1.5 eV. DFT calculations were thus undertaken to understand the origin of the broad preedge feature in the experimental spectrum.

TD-DFT calculations done on the $[CrO(L)_2]^{1-}$ anion reproduce the broad feature in the preedge region. The calculated absolute energies are, however, found to be lower in energy by 61 eV than the experimental values. This is because of the restriction of the DFT methods in defining the absolute energies of the core orbitals which mainly determine the S K-edge transition energies. The calculated spectrum shown in Figure 11 is thus shifted by 61 eV so that a direct comparison can be made with the experiment.

Five preedge transitions are calculated in the energy range of 2468−2472 eV (corrected) from the S 1s to the Cr 3d orbitals. Thus, a reasonable, although not conclusive, interpretation of the experimental result is that the experimental spectrum consists of a superposition of five unresolved transitions. The XAS spectrum of **1** was subjected to Gaussian deconvolution in the energy range of 2468−2472 eV to simulate the individual transitions (Figure 11). Equal peak widths (0.8 eV) have been enforced in the fit. The results are summarized in Table 9. However, it is stressed that this fit is not unique because of the limited resolution of the experimental data. Nevertheless, the calculations nicely reproduce the relative intensities and energies of the individual transitions (Figure 11 and Table 9). The intensity of the preedge transitions is found to be directly related to the extent of metal−ligand covalency, as has been concluded previously on the basis of the theoretical studies.[27−29] The most intense transition in the region of peak 4 (2470.5), corresponds to a transition to the Cr $3d_{xy}$ ($7a''$) orbital, which is strongly antibonding with the sulfur σ-orbitals. Because of the ligand geometry, the overlap between these orbitals is very favorable and provides an efficient pathway for the ligand-to-metal electron donation. The total sulfur p character

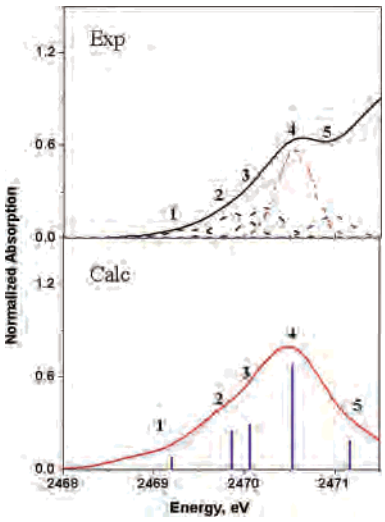

Figure 11. Deconvoluted S K-edge X-ray absorption spectrum of **1** (top) in the preedge region and its comparison to that of the calculated S K-edge X-ray absorption spectrum of the $[CrO(L)_2]^{1-}$ anion as obtained from BP86 time-dependent density functional calculations.

Table 9. Analysis of the Preedge Transitions for $[CrO(L)_2]^{1-}$ Following Gaussian Deconvolution of the S K-edge Spectrum in the Preedge Region Shown in Figure 11 Combined with the Results of the Time-Dependent Density Functional Calculations at the Scalar Relativistic ZORA BP86 Level

	energy (eV)		relative intensities[a]			
peak	exptl	calcd (+61 eV)	exptl	calcd	assignment	S 3p (%)
1	2469.32	2469.12	0.143	0.181	S 1s → 5a′($d_{x^2-y^2}$)	4.8
2	2469.90	2469.88	0.306	0.330	S 1s → 6a′(d_{xz})	9.7
3	2470.20	2470.07	0.329	0.371	S 1s → 6a″(d_{yz})	10.0
4	2470.57	2470.57	1.000	1.000	S 1s → 7a″(d_{xy})	34.7
5	2470.97	2471.20	0.172	0.210	S 1s → 7a′(d_{z^2})	6.1

[a] With respect to the most intense transition (band 4) whose intensity is taken as unity.

in this orbital is calculated to be 34.7%. The remaining four 3d orbitals are significantly less covalent than the $3d_{xy}$ orbital (Table 6). The preedge transitions to these orbitals (transitions 1, 2, 3, and 5) thus appear with much smaller intensities than peak 4 (Table 9).

Conclusion

In the present study, the electronic structures of oxo-bis(benzene-1,2-dithiolato)chromate(V) complexes **1** and **2** have been investigated in some detail experimentally and theoretically. An important structural feature of these complexes is the different dihedral angles (φ) between the mean trapezoidal C−S−S−C and the Cr−S−S planes on the two sides of the chromium atom. The angles differ by a constant value of ∼20° in both **1a** and **2**. Calculations at the DFT level on the $[CrO(L)_2]^{1-}$ anion reveal that its C_s geometry is energetically favored over a more symmetric C_{2v} structure because of strong S(3p) → Cr($3d_{x^2-y^2}$) π-donation. Constraining the molecular geometry to C_{2v} diminishes this favorable metal−ligand bonding interaction, as the sulfur p_z orbitals remain almost orthogonal to the singly occupied Cr $3d_{x^2-y^2}$ orbital. Analysis of the electronic spectra of the complexes identify the presence of the low-lying ligand to metal charge-transfer excited states, which are responsible for making the principal g value in the EPR spectrum larger than the free-electron g value. The XAS spectral analysis in **1** is consistent with the Cr(V) assignment for the complex. The S K-edge spectrum reveals a broad feature centered around 2470.5 eV, which is assigned as the superposition of five individual preedge transitions to the Cr 3d manifold engaged in covalent interaction with the sulfur atoms.

Acknowledgment. We are grateful to the Fonds der Chemischen Industrie for financial support. SSRL operations are funded by the Department of Energy, Office of Basic Energy Sciences. The Structural Molecular Biology program is supported by the National Institutes of Health, National Center for Research Resources, Biomedical Technology Program, and by the Department of Energy, Office of Biological and Environmental Research. R.K., K.R., and I.S. thank the Max-Planck Society for a stipend.

Supporting Information Available: Figure S1 showing the disorders in the crystal structures of **1a**·2CH3CN and **2**, Figure S2 showing the simulated EPR spectrum of **1** in a frozen CH_2Cl_2 solution at 10K, Figure S3 showing the temperature dependence of the MCD spectra of **1**, Table S1 showing the atomic charges and the spin density distribution in $[CrO(L)_2]^{1-}$ as obtained from ZORA B3LYP DFT calculations, and complete listings of crystallographic details, atom coordinates, bond lengths and angles, thermal displacement parameters, and calculated positional parameters for complexes **1a** and **2**. This material is available free of charge via the Internet at http://pubs.acs.org.

IC051844S